Quantum particle in a parabolic lattice in the presence of a gauge field

Andrey R. Kolovsky,[1] Fabian Grusdt,[2,3] and Michael Fleischhauer[2]

[1]*Kirensky Institute of Physics, 660036 Krasnoyarsk, Russia and Siberian Federal University, 660041 Krasnoyarsk, Russia*
[2]*Department of Physics and Research Center OPTIMAS, University of Kaiserslautern, D-67663 Kaiserslautern, Germany*
[3]*Graduate School Materials Science in Mainz, D-67663 Kaiserslautern, Germany*

We analyze the eigenstates of a two-dimensional lattice with additional harmonic confinement in the presence of an artificial magnetic field. While the softness of the confinement makes a distinction between bulk and edge states difficult, the interplay of harmonic potential and lattice leads to a different classification of states in three energy regions: In the low-energy regime, where lattice effects are small, all states are transporting topologically nontrivial states. For large energies above a certain critical value, the periodic lattice causes localization of all states through a mechanism similar to Wannier-Stark localization. In the intermediate energy regime transporting, topologically nontrivial states coexist with topologically trivial countertransporting chaotic states. The character of the eigenstates, in particular their transport properties, are studied numerically and are explained using a semiclassical analysis.

I. INTRODUCTION

Ultracold atoms in optical lattices have established themselves as powerful model systems offering unique experimental facilities for studying many fundamental phenomena of solid-state and many-body physics. For example, the near absence of dissipation in optical lattices has led to the observation of single-particle quantum interference effects, such as Bloch oscillations or Landau-Zener tunneling [1–3], as well as Anderson localization in a disorder potential [4]. The ability to tune interactions, e.g., by spatial confinement made it possible to drive interaction-induced quantum phase transitions in cold atom experiments [5] and the variety of lattice geometries possible allows one to observe, e.g., magnetic frustration in triangular lattices [6].

Particularly interesting in this context is the recent experimental realization of artificial magnetic fields in lattices [7–10] that opens prospects for studying quantum Hall effects and Chern insulators with neutral atoms. To understand how well this system can reproduce the solid-state Hall physics and what novel effects may arise in the cold-atom setting, it is important to understand the role of boundary conditions that principally differ from the Dirichlet boundary conditions in solid crystals. This problem was addressed recently in [11–14], where a quantum particle in a two-dimensional (2D) square lattice subject to an Abelian gauge field was considered and the effects of a confinement potential $V(\mathbf{r}) \sim (x^\delta + y^\delta)$ [11] and $V(\mathbf{r}) \sim r^\delta$ [12–14] was studied. These potentials impose smooth boundaries with a variable steepness characterized by the parameter δ. It was shown that there is no principle difference between Dirichlet ($\delta = \infty$) and smooth boundaries if $\delta \geqslant 4$. For $\delta \geqslant 4$ one can clearly distinguish edge states from bulk Landau states which is believed to be a precondition to mimic solid-state Hall physics with cold atoms. The case $\delta = 2$, which is typically realized in laboratory experiments, appeared to be more subtle, with no clear conclusions and contradictory statements that separation between the edge and bulk states is possible [13] or not [11].

The aim of the present work is a detailed analysis of the spectrum and eigenstates of a quantum particle (an atom) in a 2D lattice with harmonic confinement (so-called parabolic lattice [15]) in the presence of an artificial magnetic field (see Fig. 1). In other words, we focus on the above-mentioned case of $\delta = 2$. Without lattice potential, the eigenstates are identical to Landau levels (LLs) in symmetric gauge. If the harmonic confinement is weak, such that the oscillator frequency is small compared to the cyclotron frequency, every eigenstate with energy E corresponding to lowest LL states is localized at the boundary of the classically allowed region fixed by E, and it makes no sense to distinguish edge and bulk states. Numerical simulations of eigenstates and spectra, of wave-packet dynamics, and the effect of a local flux insertion show, however, that the presence of a lattice potential gives rise to a different classification of eigenstates in three regimes: a low-, medium-, and high-energy regime. The structure of the corresponding eigenstates will be explained making use of a semiclassical analysis as well as recent analytical results about Landau-Stark states [18,19], which are eigenstates of a quantum particle in the presence of a "magnetic" field normal to the lattice plane and an in-plane "electric" field. We will introduce a classification of quantum states into topologically nontrivial transporting states, chaotic countertransporting states, and localized states. We also identify a fundamental frequency [the encircling frequency; see Eq. (7) in Sec. III], which takes over the role of cyclotron frequency for the quantum particle in a plane lattice.

II. MODEL

We consider neutral atoms in a a two-dimensional square lattice with period $a = 1$ in the tight-binding limit, as indicated in Fig. 1. The atoms are subject to an artificial magnetic field and there is an additional harmonic confinement. Using the Landau gauge the corresponding Hamiltonian reads

$$(\widehat{H}\psi)_{n,m} = -\frac{J}{2}(e^{i2\pi\alpha n}\psi_{n,m+1} + e^{-i2\pi\alpha n}\psi_{n,m-1})$$
$$-\frac{J}{2}(\psi_{n+1,m} + \psi_{n-1,m}) + \frac{\gamma}{2}(n^2 + m^2)\psi_{n,m},$$
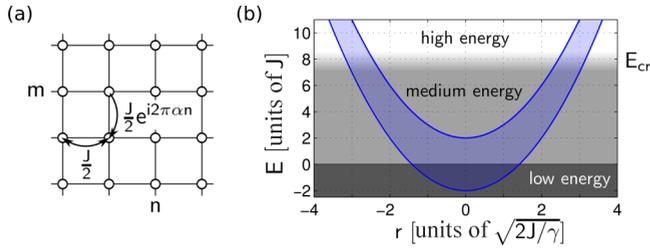$$(1)$$

FIG. 1. (Color online) (Left) Two-dimensional square lattice model with complex hopping amplitudes equivalent to a magnetic field perpendicular to the lattice. There is an additional harmonic confinement potential as is the case for most cold-atom experiments. The Peierls phase α quantifies the flux per plaquette in units of the flux quantum. (Right) Shaded region between parabolas (blue): sketch of allowed spatial and energy regions for particle trajectories in local density approximation and for $\alpha = 0$. Characteristic energy scales that will be introduced in the paper are the minimum energy $E \approx -2J$ (lower solid parabola), the energy $E = 0$ where chaotic trajectories appear (central dashed parabola), and E_{cr} where a delocalization-localization crossover takes place.

where n and m label the sites of the square lattice, J is the hopping matrix element, and γ the strength of harmonic confinement. (The latter parameter can be expressed through the trap frequency ω_{hc} and the atom mass M as $\gamma = Ma^2\omega_{\mathrm{hc}}^2$.) The presence of the magnetic field is encoded in the Peierls phase α which is equal to the magnetic flux per plaquette in units of the flux quantum. In order to be close to Landau-level physics in a homogeneous system, we will assume throughout this paper that the magnetic unit cell is much larger than the lattice unit cell. In most cases we use $\alpha = 1/6$ or $1/10$.

III. NUMERICAL SIMULATION OF THE QUANTUM PROBLEM

A. Eigenstates and spectrum

If $\gamma = 0$ the spectrum of (1) consists of a finite (rational α) or infinite (irrational α) number of magnetic sub-bands in the energy interval $-2J < E < 2J$. The presence of the harmonic confinement changes this spectrum. It is now unbounded from above, $-2J < E < \infty$, and one finds only remnants of the magnetic sub-bands in the form of steps in the mean density of states (DOS) for $E < 2J$ [20]. With increase of the energy above $2J$ the mean density of states approaches the value,

$$\rho(E) = 2\pi/\gamma, \qquad (2)$$

which coincides with the density of states of (1) for $\alpha = 0$. Although $\rho(E)$ for $\alpha \neq 0$ looks similar to that for $\alpha = 0$, the details of the spectrum and the eigenstates are completely different.

If γ is small and $\alpha = 0$, a qualitative picture of the effect of the harmonic confining potential can be obtained by treating it as a space-dependent chemical potential, which leads to the overall band structure depicted in Fig. 1. As indicated in the figure we will show in this paper that one has to distinguish three qualitatively different energy regions: a low-energy regime $E < 0$, a high-energy regime $E > E_{\mathrm{cr}} > 2J$, and a medium energy regime in between. The critical energy will be
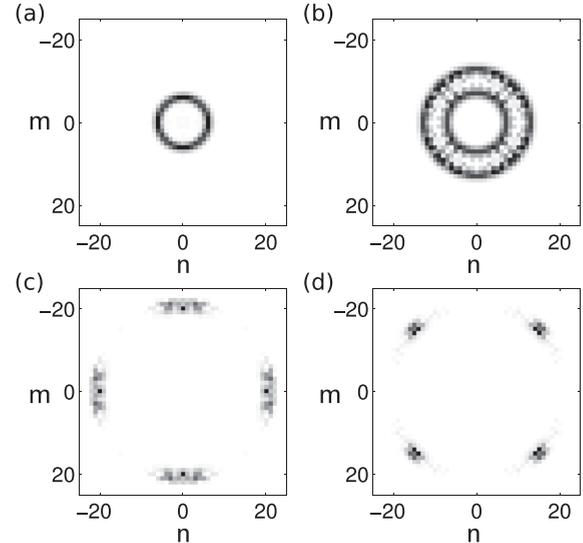

FIG. 2. The 25th (a), 349th (b), 1365nd (c), and 1370th (d) eigenstates of the Hamiltonian (1) with energies $E/J = -0.5511$, $2.7671, 10.8544, 10.9069$, respectively. The squared absolute value of the wave function $\Psi_{n,m}$ is shown as a grayscale map. We used $\alpha = 1/6$ and $\gamma/J = 0.05$.

shown to be

$$E_{\mathrm{cr}} = \frac{(2\pi\alpha J)^2}{2\gamma} = E_R\left(\frac{\omega_\alpha}{\omega_{\mathrm{hc}}}\right)^2, \qquad (3)$$

where $E_R = \hbar^2/Ma^2$ is proportional to the recoil energy and $\omega_\alpha = 2\pi\alpha J/\hbar$ has the meaning of the cyclotron frequency. As will be seen in the following, the nature of the eigenstates is very different in the different parts of the spectrum.

Numerical diagonalization of the Hamiltonian Eq. (1) allows us to easily calculate the single-particle spectrum and the corresponding eigenstates of the problem. In Fig. 2 we have plotted the absolute square of the eigenstates for energy values corresponding to the different regions. One notices a qualitative change in the character of the states when increasing the energy. For low energies, as shown in Fig. 2(a) ($E/J = -0.5511$), the eigenstates are circular, resembling Landau states with fixed angular momentum. For intermediate energies, as shown in Fig. 2(b) ($E/J = 2.7671$) there is a more complex pattern. There are two circular structures, an inner and an outer one, corresponding to the boundaries of the classically allowed regions for the given energy [see Fig. 1(b)]. In addition there is, however, also a finite probability amplitude in the spatial region between the two rings. Finally when going to high energies, as shown in Figs. 2(c) and 2(d) localized structures emerge with a fourfold symmetry corresponding to the underlying square lattice.

1. Low-energy region

In the low-energy part of the spectrum we can use the long-wavelength or effective mass approximation to write the Hamiltonian, Eq. (1), in the form (here and in the following
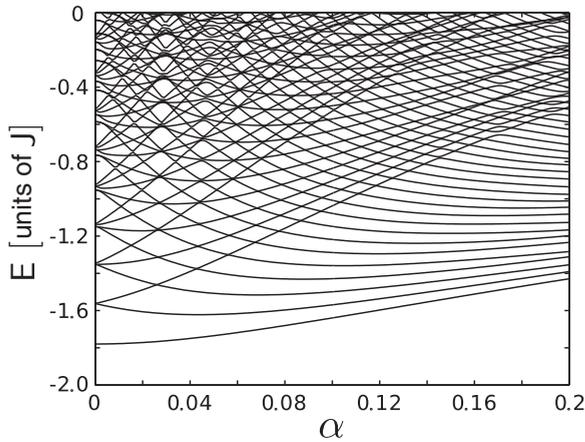
FIG. 3. The low-energy part of the spectrum for $J = 1$ and $\gamma = 0.05$ as a function of the Peierls phase α.

we set $\hbar = 1$),

$$\widehat{H} = \frac{1}{2M^*}(\hat{\mathbf{p}} - \mathbf{A})^2 + \frac{\gamma}{2}(x^2 + y^2). \qquad (4)$$

Here $M^* = J^{-1}$ is the effective mass, and $\mathbf{A} = 2\pi\alpha(-y/2, x/2)$ the vector potential (where we have changed to the symmetric gauge). It is convenient to express (4) in the form,

$$\widehat{H} = \widehat{H}_0 - \omega\widehat{L}_z, \quad \widehat{H}_0 = \frac{\hat{\mathbf{p}}^2}{2M^*} + \frac{\gamma + M^*\omega^2}{2}(x^2 + y^2), \qquad (5)$$

where $\widehat{L}_z$ is the angular-momentum operator, and $\omega = J\pi\alpha$. The eigenstates of (5) are labeled by the angular momentum n_L, and the radial quantum number n_r, defining the Landau level [21]. These quantum numbers can be used to characterize the low-energy eigenstates of the system (1) in spite of the fact that, strictly speaking, the eigenstates do not possess rotational symmetry due to the lattice potential.

Figure 3 shows the lower part of the energy spectrum of (1) as the function of the Peierls phase α, i.e., the magnetic flux per plaquette. One clearly sees the Zeemann splitting of degenerate levels of the 2D harmonic oscillator, where the first level has quantum numbers $(n_r, n_L) = (0, 0)$, the second level $(0, 1)$ and $(1, -1)$, the third $(0, 2)$, $(1, 0)$, $(2, -2)$, the fourth $(0, 3)$, $(1, 2)$, $(2, -1)$, $(3, -3)$, the fifth $(0, 4)$, $(1, 2)$, $(2, 0)$, $(3, -2)$, $(4, -4)$, and so on. With increase of α these levels rearrange in a pattern which consists of series of levels with fixed n_r and monotonically increasing n_L.

A different interpretation of the low-energy spectrum is based on the observation that for $\gamma = 0$ the Hamiltonian (5) defines the degenerate Landau levels with level spacing given by the cyclotron frequency,

$$\omega_\alpha = 2\pi\alpha J = 2\omega, \quad |\alpha| \ll 1/2. \qquad (6)$$

The harmonic confinement splits these degenerate levels into series of levels with equidistant spacing Ω. For small γ one finds

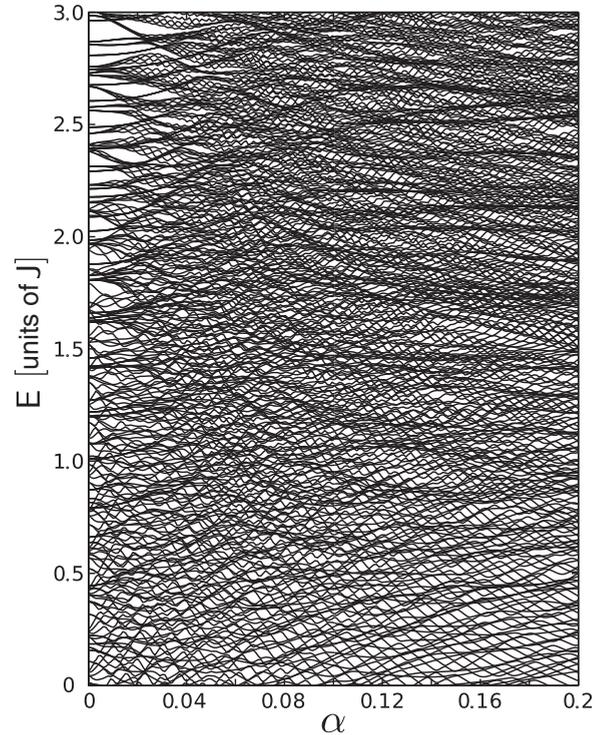$$\Omega = \frac{\gamma}{2\pi\alpha}. \qquad (7)$$

FIG. 4. A fragment of the medium energy spectrum of the Hamiltonian (1) for $J = 1$, $\gamma = 0.05$, and $0 \leqslant \alpha \leqslant 0.2$.

2. Medium energy region

Figure 4 shows a fragment of the medium energy spectrum of Hamiltonian (1) as a function of the Peierls phase α for $J = 1$ and $\gamma = 0.05$. Here a rather complicated level pattern is noticed. There is a large number of levels with true or nearly avoided crossings. One notices, however, that some regular structures of the low-energy spectrum survive.

3. High-energy region

The characteristic feature of the high-energy spectrum above a certain critical value E_{cr}, a fragment of which is shown in Fig. 5, is an approximate fourfold degeneracy of the energy levels. This degeneracy reflects localization of the eigenstates
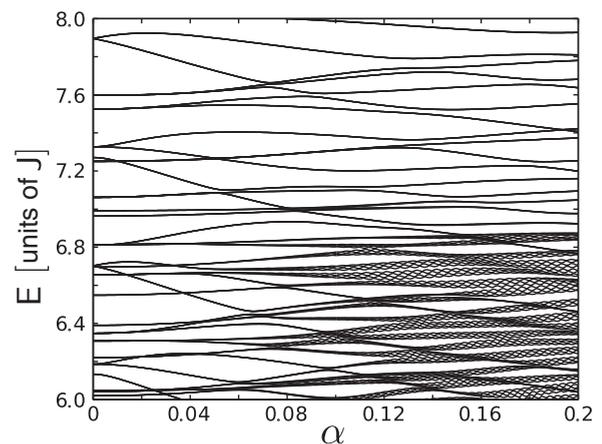

FIG. 5. A fragment of the high-energy spectrum of the Hamiltonian (1), for $J = 1$, $\gamma = 0.05$, and $0 \leqslant \alpha \leqslant 0.2$
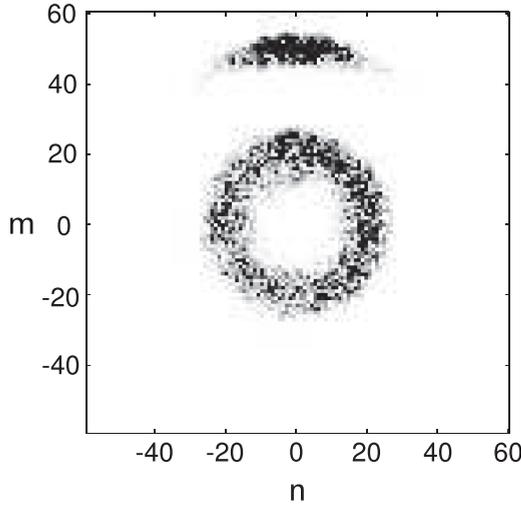
FIG. 6. Populations of the lattice sites at the end of numerical simulation. Initial conditions correspond to a narrow scrambled Gaussian centered at $(n_0, m_0) = (0,20)$, case (a), and $(n_0, m_0) = (0,50)$, case (b). Parameters are $J = 1$, $\alpha = 0.1$, and $\gamma = 0.01$. Evolution time is $t = 30T_J$, $(T_J = 2\pi/J)$.

in segments of the circles [see Fig. 2(d)]. Due to the fourfold lattice symmetry there are three other eigenstates with almost the same energy which look similar to the depicted state. From this set of four exact states one can construct a new set of four approximate eigenstates, where every state is localized only in one segment. Thus a particle with the mean energy $E > E_{cr}$, which is initially localized within one of the segments, remains localized in this segment for exponentially large times.

B. Dynamical signatures of localization

To experimentally observe the characteristics of eigenstates at different energies, we suggest measuring dynamics of an initially localized wave packet. Our numerical experiment follows the scheme of laboratory experiments on dipole oscillations of cold atoms in parabolic lattices. The protocol involves a sudden shift of the origin of the harmonic potential by distance r_0, so that the atomic cloud appears on the slope of the parabolic lattice where it has the energy $E \approx \gamma r_0^2/2$. Then the system evolves freely for a certain time t, which is followed by (destructive) measurement of the atomic density. The result of this numerical experiment is shown in Fig. 6, where we have chosen a narrow Gaussian distribution with random phases as the initial condition. The packet is shifted from the lattice origin by $m_0 = 20$ sites, case (a), and $m_0 = 50$ sites, case (b). In the former case the packet energy is smaller than the critical energy E_{cr} and it encircles the lattice origin. In the latter case, where $E > E_{cr}$, the wave packet remains localized. Since the wave-packet dynamics can be expressed in terms of eigenstates, this result undoubtedly indicates the qualitative difference between states below and above E_{cr}.

C. Effects of disorder

An important characteristics of topological systems is their robustness against disorder. Because of their effective description in terms of the topologically nontrivial lowest

Landau level states (cf. Sec. III A 1), we expect low-energy states to be robust to such disorder. In the following we will show that this is indeed the case, while high-energy states are very sensitive to disorder.

To this end we analyze the robustness of these states by adding a weak random on-site potential V_{nm} to the Hamiltonian (1) in our numerical simulations. V_{nm} is a uniform distribution with vanishing mean value and is assumed to be spatially uncorrelated,

$$[\overline{V_{nm}V_{n'm'}}]^{1/2} = \epsilon \, \delta_{n,n'}\delta_{m,m'}. \tag{8}$$

Here ϵ describes the strength of the disorder potential. A convenient characteristic of the robustness of an eigenstate $\Psi^{(\nu)}$ to disorder is the quantity,

$$C^{(\nu)} = \left| \sum_{n,m} \Psi_{-n,-m}^{(\nu)} \left(\Psi_{n,m}^{(\nu)} \right)^* \right| \leqslant 1, \tag{9}$$

where the sum runs over all lattice sites. For a vanishing random potential one can prove using Eq. (1) that all eigenstates are symmetric or antisymmetric functions with respect to reflection $n \to -n$ and $m \to -m$, i.e.,

$$\Psi_{-n,-m} = \pm \Psi_{n,m}. \tag{10}$$

In this case $C^{(\nu)}$ equals to unity and

$$\Gamma(E) = \sum_{\nu, E_\nu \leqslant E} C^{(\nu)} \tag{11}$$

is equal to the integrated density of states up to energy E.

Figure 7 shows $\Gamma(E)$ for increasing disorder strength as well as the corresponding function in the absence of disorder (dashed curve). The random potential breaks the symmetry (10) and $C^{(\nu)}$ quickly drops below unity (see inset of Fig. 7), where the eigenstates are sorted according to their energies. One notices a remarkable agreement of $\Gamma(E)$ with
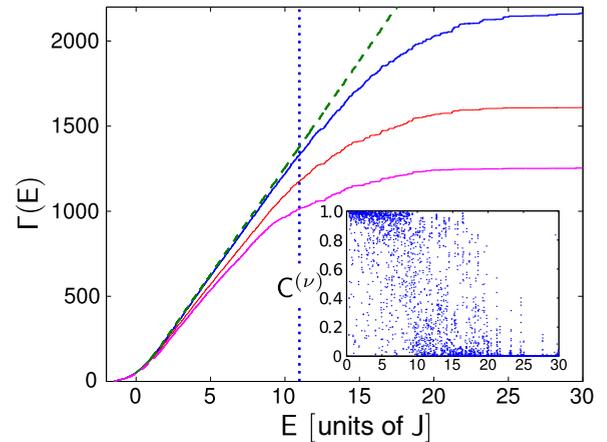

FIG. 7. (Color online) (Main panel) Effect of disorder on the eigenstates. Shown is the cumulative sum $\Gamma(E) = \sum_\nu C^{(\nu)}$ for different disorder strength $\epsilon/J = 0.01$, 0.05, 0.1, solid lines from top to bottom. The vertical (blue) dotted line indicates the critical energy and the (green) dashed line shows the integrated DOS in the absence of disorder. (Inset) The quantity (9) for a specific realization of a weak on-site random potential $|V_{n,m}| \leqslant \epsilon/2$ with $\epsilon = 0.1J$. The eigenstates are ordered by their energies E. We used $\alpha = 1/6$ and $\gamma/J = 0.05$.

its value in the absence of disorder in the low-energy region. The deviations from the disorder-free curve increase with increasing ϵ but stay small until the critical energy E_{cr}. Thus the random potential affects only some of the eigenstates for $E < E_{cr}$. Above E_{cr}, however, $\Gamma(E)$ saturates which indicates that the disorder completely randomizes the eigenstates. We conclude that most of the states with $E_\nu < E_{cr}$ are robust against impurities ($C^{(\nu)} \approx 1$) while most of the states with $E_\nu > E_{cr}$ are not ($C^{(\nu)} \approx 0$). Let us emphasize that at E_{cr} a crossover takes place, rather than a sharp transition.

In the following sections we want to provide some understanding of the spectrum, the eigenstates, and their transport properties for $\alpha \neq 0$.

IV. CLASSICAL APPROACH

Following the line of Refs. [18,19] we provide here a classical analysis of the system (1), which allows insight into the transport properties of the states. The classical counterpart of the quantum Hamiltonian (1) reads

$$H_{cl} = -J\cos(p_x) - J\cos(p_y - \tilde{x}) + \frac{\tilde{\gamma}}{2}(\tilde{x}^2 + \tilde{y}^2), \quad (12)$$

where $\tilde{\gamma} = \gamma/(2\pi\alpha)^2$. As shown in [19] the classical limit corresponds to $\alpha \to 0$ while keeping $\tilde{\gamma}$ constant, and in this case $2\pi\alpha n \to \tilde{x}$ and $2\pi\alpha m \to \tilde{y}$ become continuous variables. Thus the only relevant parameter of the classical dynamics is $\tilde{\gamma}/J$ [22]. In what follows, however, we shall use a different form of the classical Hamiltonian,

$$H_{cl} = -J\cos(p_x) - J\cos(p_y - 2\pi\alpha x) + \frac{\gamma}{2}(x^2 + y^2), \quad (13)$$

which is obtained from the previous Hamiltonian by obvious scaling of the coordinates x and y. This form allows a direct comparison of the classical trajectories with the quantum wave functions for a finite α.

For a given energy E any phase trajectory of (13) is uniquely described by momenta p_x and p_y and the angle $\vartheta = \arctan(x/y)$, which are cyclic variables. Thus the energy shell of (13) lies inside the three-dimensional torus or coincides with this torus if $E \geqslant 2J$. Figure 8 shows the Poincare cross sections of the energy shell by the plane $\vartheta = 0$ for few values of E. While for $E < 0$ we only found regular trajectories, for $E \geqslant 0$, where the effective mass approximation (4) fails completely due to the lattice, the typical structure of a nonintegrable system with mixed phase space is noticed.

Let us first discuss the case of moderate energy, where the phase space consists of two big stability islands surrounded by the chaotic sea [see Fig. 8(c)]. For reasons that become clear below, we will refer to them as inner and outer transporting islands. The blue and red lines in Fig. 9 show the particle trajectories for initial conditions inside the central and lower or upper stability islands, respectively. Additionally, the winding angle $\vartheta = \arctan(x/y)$ is depicted in Fig. 10(a) as a function of time. It is seen from Fig. 10 that both of these trajectories encircle the coordinate origin clockwise with frequency Ω given in Eq. (7). We will refer to them as *transporting* trajectories.

In the classical approach the encircling frequency is determined by the drift velocity of a charged particle in the crossing electric and magnetic fields. In fact, locally we can approximate the parabolic potential by a gradient force
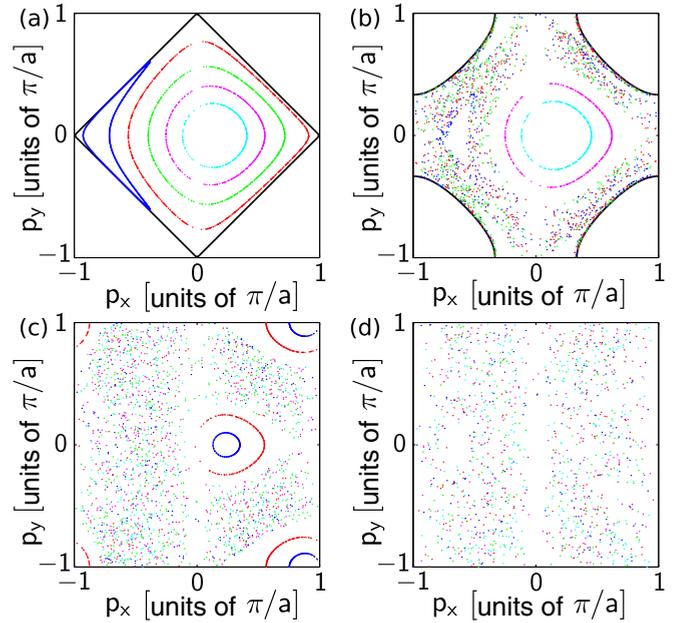

FIG. 8. (Color online) Poincare cross sections by the plane $\vartheta = 0$ for energy $E/J = 0, 0.5, 3, 11$ (a)–(d). The system parameters are $\alpha = 1/6$ and $\gamma/J = 0.05$. The solid lines in the panels (a) and (b) restrict the available phase space.

pointing to the coordinate origin,

$$\mathbf{F} = -\gamma\mathbf{r}, \quad \mathbf{r} = (x, y). \quad (14)$$

In the notation used throughout the paper, the drift velocity in the direction perpendicular to $\mathbf{F}$ is given by [18]

$$v^* = F/2\pi\alpha. \quad (15)$$

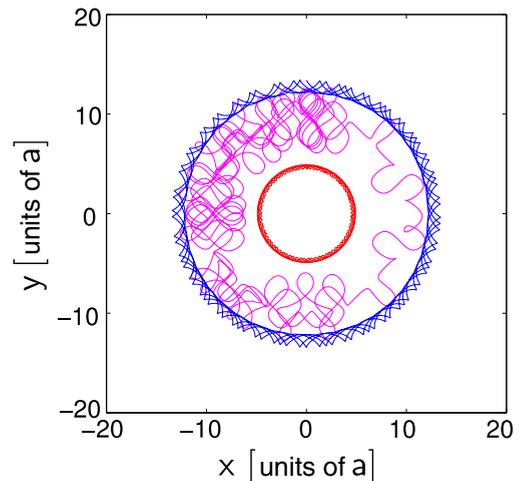Thus the encircling period is $T_\Omega \equiv 2\pi/\Omega = 2\pi r/v^* = (2\pi)^2\alpha/\gamma$.

FIG. 9. (Color online) Examples of classical trajectories with $E/J = 2.5$ for three different initial conditions: $(p_x, p_y) \approx (0,0)$ (outer, blue), (π,π) (inner, red), and $(\pi/2, \pi/2)$ (middle, magenta). The initial value of x is zero for all three trajectories and the initial value of y is adjusted to ensure equal energies. The evolution time corresponds to five periods of frequency (7). We used parameters $\alpha = 1/6$ and $\gamma/J = 0.05$.
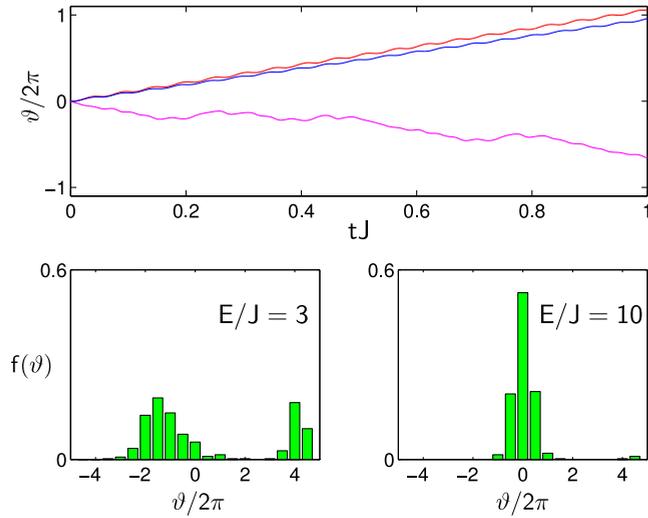
FIG. 10. (Color online) (Upper panel) Winding angle $\vartheta = \arctan(x/y)$ as the function of time for the three trajectories shown in Fig. 9. Upper curve is the inner regular trajectory, middle curve the outer regular trajectory, and the lower curve the chaotic trajectory. (Lower panels) Distribution function $f(\vartheta,t)$ for the winding angles ϑ at $t = 4T_\Omega = 8\pi/\Omega$ for 400 different trajectories on the energy shell $E/J = 3$ (left) and $E/J = 10$ (right).

Closer inspection of the numerical data in Fig. 10(a) shows that the encircling frequency for the outer trajectory in Fig. 9 is slightly smaller than Ω, while for the inner trajectory it is slightly larger. More importantly the inner trajectories appear only when E approaches $2J$. Let us mention that angular momentum is an approximate integral of motion for the transporting trajectories as $\dot{\vartheta} \approx$ const. and $r \approx$ const. [see Figs. 9 and 10(a)], and as

$$\dot{\vartheta} = \frac{L}{r^2}, \quad L = \dot{\mathbf{r}} \times \mathbf{r}. \quad (16)$$

If the initial condition is chosen outside the transporting islands [magenta lines in Figs. 9 and 10(a)], yet another type of trajectory is found. These trajectories appear to be chaotic, and in average rotate counterclockwise. We will refer to them as *countertransporting* trajectories. Because of their chaotic nature, they do not have a well-defined encircling frequency. Instead we find numerically for sufficiently large energies that they obey the so-called summation rule. Namely, if we chose an ensemble of classical particles uniformly distributed over the energy shell, the clockwise current due to (regular) transporting trajectories and the counterclockwise current due to (chaotic) countertransporting trajectories compensate each other. We conjecture that this sum rule is valid as soon as the entire phase space is classically allowed, although we are not aware of an exact proof.

The sum rule is also illustrated in the lower panels of Fig. 10 which show the distribution of the winding angles ϑ at $t = 4T_\Omega$ for 400 different trajectories with random initial conditions, yet $x(t=0) = 0$, and fixed energy $E/J = 3$ (left panel) and $E/J = 10$ (right panel). The double-peak structure of the distribution function $f = f(\vartheta,t)$ reflects the presence of both transporting and countertransporting trajectories. It is also seen in the figure that the right peak of $f(\vartheta,t)$, which is associated

with transporting trajectories, decreases if the energy is increased. This is due to the decrease of the size of transporting islands in Fig. 8, which are smaller for larger energy (i.e., larger gradient force) and completely disappear for energies above the critical energy $E_{\rm cr}$ [see Fig. 8(d)]. In this case the distribution function $f(\vartheta,t)$ becomes localized within the interval $|\vartheta| < 2\pi$, indicating the absence of transport in the system.

We can obtain an estimate for the critical energy $E_{\rm cr}$ by drawing an analogy with the related problem of Landau-Stark states which, by definition, are eigenstates of a charged particle in a two-dimensional plane lattice in the presence of in-plane electric field and normal-to-the-lattice magnetic field. It was shown in [18,19] that these states show a delocalization-localization crossover at

$$F_{\rm cr} = 2\pi\alpha J. \quad (17)$$

Namely, the localization length $\xi_\perp$ of the Landau-Stark states in the direction orthogonal to $\mathbf{F}$ blows up exponentially when the electric field decreases below the critical value (17) [23]. Associating F in (17) with the gradient force (14) and neglecting the kinetic energy in Eq. (13) we find

$$E_{\rm cr} \approx (2\pi\alpha J)^2/2\gamma. \quad (18)$$

We also mention that the classical counterpart of the quantum Hamiltonian of Landau-Stark states has quite a similar structure of phase space, containing two chains of transporting islands. In this sense, the physics behind localization of the Landau-Stark states and wave-function localization discussed in Sec. III.A is the same and is related to disappearance of the transporting islands at $F = F_{\rm cr}$.

V. TOPOLOGICAL CLASSIFICATION OF THE QUANTUM STATES

In the previous section we introduced the notions of transporting and countertransporting trajectories in the classical version of our model and identified them with the various quantum states obtained in Sec. III A. Now we will investigate the topological properties of these states. To this end we reverse Laughlin's argument [24] for the quantization of the Hall conductance: We adiabatically introduce local magnetic flux and investigate the system's response, i.e., the Hall current. This allows us to distinguish between topologically trivial and nontrivial eigenstates.

A. Local flux

A local flux insertion at the origin leads to an additional contribution to the vector potential,

$$\mathbf{A}(x,y) \sim \left(-\frac{y}{x^2 + y^2}, \frac{x}{x^2 + y^2} \right). \quad (19)$$

It corresponds to a magnetic field which is zero everywhere except at the coordinate origin. It is easy to show that the tight-binding counterpart of (19) results in an additional contribution to the Peierls phase by

$$\phi_x(n,m) \equiv \phi(n,m)$$

$$= \theta \left[\arctan\left(\frac{2n-1}{2m-1} \right) - \arctan\left(\frac{2n+1}{2m-1} \right) \right] \quad (20)$$
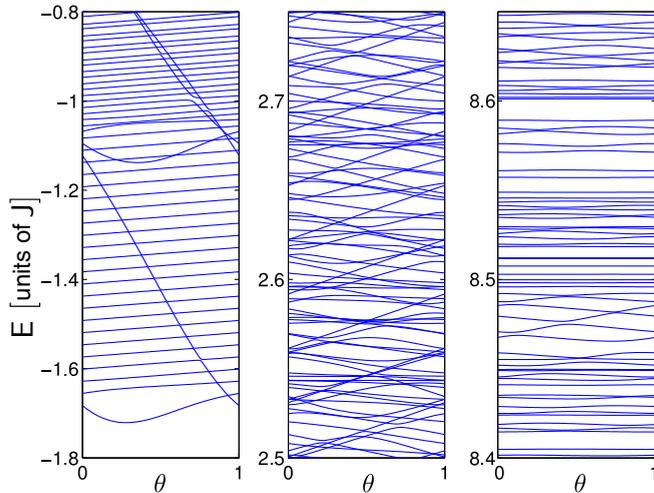
FIG. 11. (Color online) Different regions of the energy spectrum of Hamiltonian (21) as a function of the flux θ inserted at the origin. Parameters are $J = 1$, $\alpha = 0.1$, and $\gamma = 0.018$. Shown are the low- (right), medium- (middle), and high-energy regions (right). Notice the different scales of the energy axis in the panels.

in the x direction and $\phi_y(n,m) = \phi(m,n)$ in the y direction. Here θ quantifies the amount of the flux inserted in units of the magnetic flux quantum. Thus we have

$$(\widehat{H}\psi)_{n,m} = -\frac{J}{2}(e^{-i\pi\alpha m}e^{-i\phi(n,m)}\psi_{n+1,m} + \text{H.c.})$$
$$- \frac{J}{2}(e^{i\pi\alpha n}e^{i\phi(m,n)}\psi_{n,m+1} + \text{H.c.})$$
$$+ \frac{\gamma}{2}[(n - 1/2)^2 + (m - 1/2)^2]\psi_{n,m}. \quad (21)$$

Notice that in comparison with (1) we here used the symmetric gauge for the uniform magnetic field and shift the coordinate origin from the site $(n,m) = (0,0)$ to the center of the plaquette.

Figure 11 shows the low-, medium-, and high-energy parts of the spectrum of (21) as a function of the inserted flux θ. The system parameters are $J = 1$, $\alpha = 0.1$, and $\gamma = 0.018$, which correspond to the same value of the parameter $\tilde{\gamma}$ that was used in Secs. III and IV (thus also E_{cr}/J is the same as in the previous sections). It is seen from Fig. 11 that the positions of the energy levels for $\theta = 0$ and $\theta = 1$ coincide, which is a direct consequence of gauge invariance. Thus the spectrum has the cylinder topology where a given energy level is connected to another level according to some specific rule [25].

One can easily deduce this rule by analyzing the level pattern in the low-energy region [Fig. 11 (left)]. Indeed, considering $\theta = 0$ and appealing to the effective mass approximation we can assign the following quantum numbers to the depicted energy levels: $(n_r, n_L) = (0,0), (0,1), (0,2), \ldots, (0,21)$. The level spacings in this regime are described by Eq. (7). The 22nd energy level has quantum numbers $(1,-1)$ (it is the lowest-energy state belonging to the first Landau level) and next levels $(0,22), (1,0), (0,23), (1,1), (0,24), (1,2), \ldots$. When θ is increased by unity every state is seen to acquire exactly one quantum of angular momentum, as it is expected on the basis of the effective mass approximation. Moreover this is

in agreement with our expectation that low-energy states are topologically nontrivial.

This rule can also be applied to the medium energy region, however, only to the transporting states. For the transporting states, and only for those, angular momentum is an approximate quantum number. This is exemplified in the middle panel in Fig. 11, where the transporting (topologically nontrivial) states coexist with chaotic countertransporting (topologically trivial) states. One should remark though that the statement "every transporting state acquires exactly one quantum of angular momentum" is valid only if we ignore avoided crossings. The presence of avoided crossings, which reflect hybridization of the transporting and countertransporting states in the quantum case, has important consequences for the excitation dynamics of the system considered in the next subsection.

As can be seen from the right panel of Fig. 11 there is just one state that, upon flux insertion, connects to one with a larger angular momentum in the high energy region [26]. This is a signature that most of the states in this energy region are nontransporting and topologically trivial.

In conclusion, we find that in the low-energy sector of our system, all states are topologically nontrivial because they generate a nontrivial Hall current when a flux quantum is introduced to the system in the spirit of Laughlin. All states in this regime are transporting. In the high-energy sector in contrast, the system is topologically trivial with no Hall current being supported and no transporting states. In the medium energy regime we find a mixture of topologically trivial (and nontransporting) and nontrivial (transporting) states.

B. Excitation dynamics

Let us now consider excitations of the system from its ground state by a time-dependent flux $\theta = \nu t$. If ν is larger than the characteristic gap of avoided crossings but smaller than the encircling frequency Ω the system is expected to diabatically (i.e., ignoring tiny avoided crossings) follow the instantaneous energy level and, hence, the mean energy,

$$E(t) = \langle\psi(t)|\widehat{H}(\theta = \nu t)|\psi(t)\rangle, \quad (22)$$
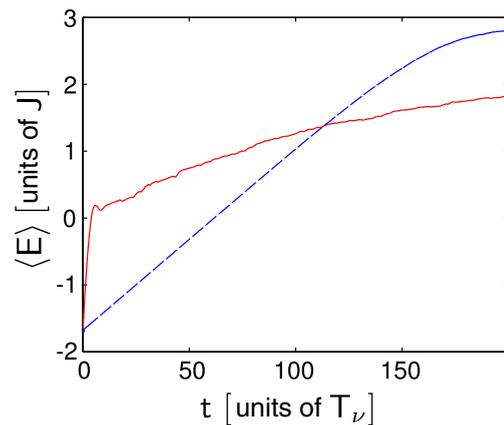

FIG. 12. (Color online) Mean energy (22) as the function of time for $J = 1$, $\nu = 0.1$, (blue) dashed line, and $\nu = -0.1$, (red) solid line. The system parameters are $\alpha = 0.1$ and $\gamma = 0.018$.
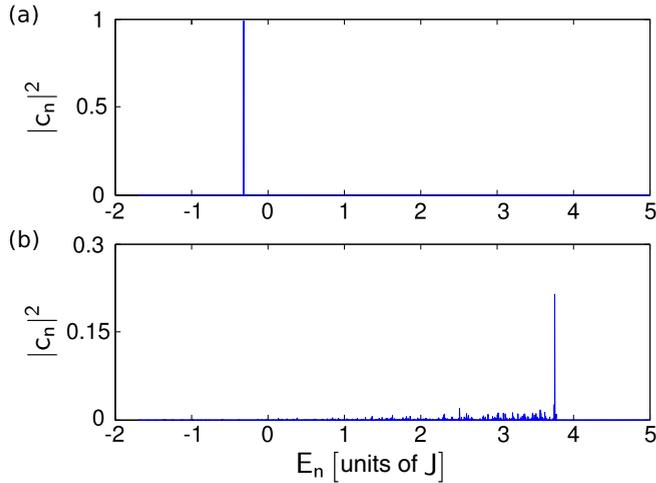
FIG. 13. (Color online) Expansion coefficients c_n for the wave function $\psi(t)$ in the instantaneous basis at $t = 50T_\nu$ and $t = 200T_\nu$ ($\nu = 0.1J$).

should monotonically grow in time. For the parameters of Fig. 11 and $\nu = 0.1J$ the average energy, Eq. (22), is shown in Fig. 12 by the blue dashed line. It is seen that for finite times $E(t)$ indeed shows the expected linear increase which for longer times, however, saturates. In the following we discuss these two regimes separately.

The linear regime corresponds to diabatic Landau-Zener transitions at the avoided crossing. This is confirmed by considering the wave function in the instantaneous basis of the Hamiltonian (21),

$$|\psi(t)\rangle = \sum_n c_n(t)|\Psi_n(\theta = \nu t)\rangle. \tag{23}$$

The upper panel in Fig. 13 shows the expansion coefficients c_n at $t = 50T_\nu$, $(T_\nu = 2\pi/\nu)$. It can be seen that only one level of the Hamiltonian $\hat{H}(\theta)$ is populated. In real space the ground-state wave function, which resembles a wide Gaussian, evolves into a ring with the radius increasing in time; see Fig. 14(a). Notice that there is no "population" inside the ring which is another indication of the diabatic regime.

When the ring is approximately two times larger than in Fig. 14(a) we observe population of the lattice sites inside the ring. This indicates that the Landau-Zener transitions at the avoided crossings are no longer diabatic and, hence, other states of $\hat{H}(\theta)$ get populated. Finally, for even larger times
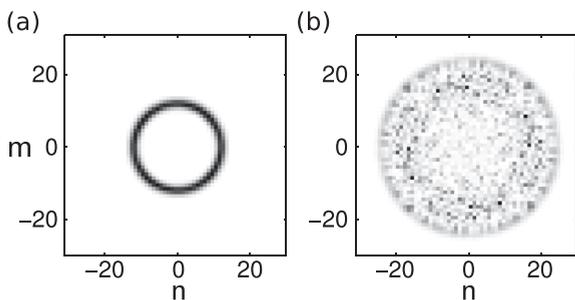
the ring fades and population is redistributed over the circle of a finite radius; see Fig. 14(b). This is the beginning of a self-thermalization process, where the mean energy $E(t)$ saturates. Remarkably, the saturation energy is found to be substantially smaller than the critical energy (18). This is a manifestation of the hybridization between transporting and countertransporting states—the system can reach $\langle E(t)\rangle \simeq E_{\mathrm{cr}}$ only in the classical limit $\alpha, \gamma \to 0$ ($\alpha^2/\gamma = \mathrm{const}$), where hybridization is absent.

We conclude this section by considering the case of negative ν. For negative ν the time-dependent flux induces a counterclockwise "circular electric field" which is expected to excite the countertransporting states. The mean energy of the system for negative $\nu = -0.1J$ is depicted by the red solid line in Fig. 12. A rapid initial growth of the energy corresponds to a transient regime where the system follows the energy level connecting the ground state $(n_r, n_L) = (0,0)$ with the state $(n_r, n_L) = (1,-1)$ in the first Landau level [see Fig. 11(a)]. After this transient regime the diabatic approximation no longer holds and the subsequent excitation dynamics resembles chaotic diffusion where population is redistributed among many eigenstates of the Hamiltonian (21), including the low-energy states (see Fig. 15). This hypothesis about chaotic diffusion is further supported by the random distribution of population of the lattice sites $|\psi_{n,m}(t)|^2$ at large times [see Fig. 16(b)].

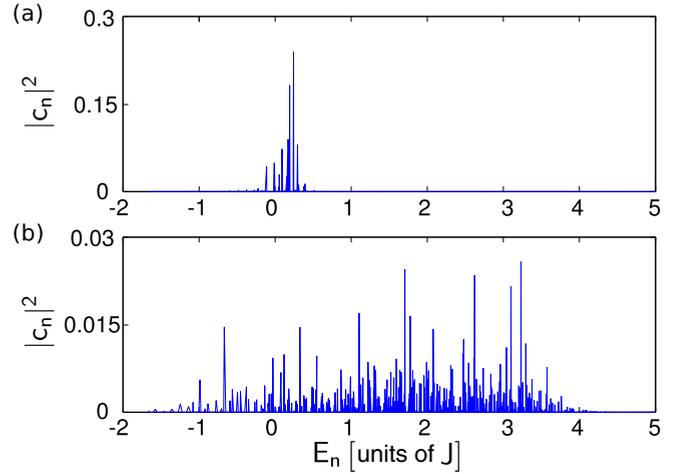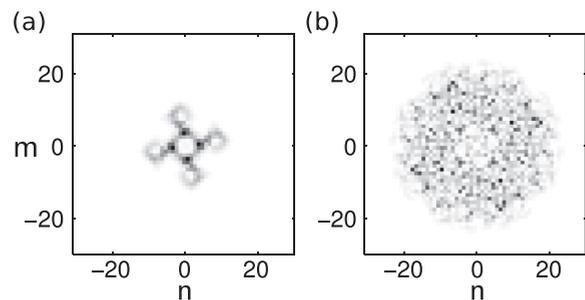

FIG. 15. (Color online) Expansion coefficients c_n for the wave function $\psi(t)$ in the instantaneous basis at $t = 5T_\nu$ and $t = 200T_\nu$ ($\nu = -0.1J$).

FIG. 14. Population of the lattice site $|\psi_{n,m}(t)|^2$ at $t = 50T_\nu$ and $t = 200T_\nu$ ($\nu = 0.1J$).

FIG. 16. Population of the lattice site $|\psi_{n,m}(t)|^2$ at $t = 5T_\nu$ and $t = 200T_\nu$ ($\nu = -0.1J$).

VI. CONCLUSIONS

We analyzed the eigenstates of a quantum particle in a parabolic lattice in the presence of a gauge field characterized by the Peierls phase α. In a simplified manner the results of this analysis can be summarized as follows.

In the absence of harmonic confinement and lattice potential the eigenstates of the problem are the well-known Landau states, which are labeled by the radial n_r (Landau level), and the angular momentum n_L quantum numbers. These Landau levels constitute sets of topologically nontrivial states. In the presence of a lattice this picture still holds in the low-energy regime of small n_r (in particular, $n_r = 0$) and positive n_L (for positive α), where the effective mass approximation is valid. We specifically showed that all characteristic features carry over: Low-energy states are extended, robust against disorder, and they produce a quantized Hall current when flux is locally inserted in the center of the lattice. Classically, they correspond to regular transporting trajectories.

In the presence of the harmonic confinement (with strength γ), these Landau states arrange in an equidistant spectrum with frequency separation $\Omega = \gamma/2\pi\alpha$ between two states whose angular momentum n_L differs by one unit. When also the lattice is present, we find three sorts of states: the low-energy sector can still be understood in terms of Landau states described above. When the energy increases the discreteness of the lattice starts to break the effective mass approximation. In the classical picture, more and more transporting trajectories turn into chaotic ones, and the corresponding quantum states can be labeled only by their energies. These states are sensitive to disorder and topologically trivial, as we deduced from their response to local flux insertion. In the medium energy sector we furthermore identified a second set of regular transporting trajectories (classical picture), which in the quantum picture are obtained from the negative-effective mass approximation around the band maximum. In the high-energy sector, above the critical energy E_{cr}, all states become localized due to the Landau-Stark localization. Hence, in this regime there is no transport in the system (i.e., the system becomes a trivial insulator) and the eigenstates are topologically trivial.

[1] M. Ben Dahan, E. Peik, J. Reichel, Y. Castin, and C. Salomon, Phys. Rev. Lett. **76**, 4508 (1996).

[2] E. Haller, R. Hart, M. J. Mark, J. G. Danzl, L. Reichsollner, and H.-C. Nägerl, Phys. Rev. Lett. **104**, 200403 (2010).

[3] A. Zenesini, H. Lignier, G. Tayebirad, J. Radogostowicz, D. Ciampini, R. Mannella, S. Wimberger, O. Morsch, and E. Arimondo, Phys. Rev. Lett. **103**, 090403 (2009).

[4] G. Roati, C. D' Errico, L. Fallani, M. Fattori, C. Fort, M. Zaccanti, G. Modugno, M. Modugno, and M. Inguscio, Nature (London) **453**, 895 (2008).

[5] M. Greiner, O. Mandel, T. Esslinger, T. W. Hänsch, and I. Bloch, Nature (London) **415**, 39 (2002).

[6] J. Struck, C. Ölschläger, R. Le Targat, P. Soltan-Panahi, A. Eckardt, M. Lewenstein, P. Windpassinger, and K. Sengstock, Science **333**, 996 (2011).

[7] M. Aidelsburger, M. Atala, S. Nascimbéne, S. Trotzky, Y.-A. Chen, and I. Bloch, Phys. Rev. Lett. **107**, 255301 (2011).

[8] J. Struck, C. Ölschläger, M. Weinberg, P. Hauke, J. Simonet, A. Eckardt, M. Lewenstein, K. Sengstock, and P. Windpassinger, Phys. Rev. Lett. **108**, 225304 (2012).

[9] M. Aidelsburger, M. Atala, M. Lohse, J. T. Barreiro, B. Paredes, and I. Bloch, Phys. Rev. Lett. **111**, 185301 (2013).

[10] H. Miyake, G. A. Siviloglou, C. J. Kennedy, W. C. Burton, and W. Ketterle, Phys. Rev. Lett. **111**, 185302 (2013).

[11] M. Buchhold, D. Cocks, and W. Hofstetter, Phys. Rev. A **85**, 063614 (2012).

[12] N. Goldman, J. Beugnon, and F. Gerbier, Phys. Rev. Lett. **108**, 255303 (2012).

[13] N. Goldman, J. Beugnon, and F. Gerbier, Eur. Phys. J. Special Topics **217**, 135 (2013).

[14] N. Goldman, J. Dalibard, A. Dauphin, F. Gerbier, M. Lewenstein, P. Zoller, and I. B. Spielman, Proc. Natl. Acad. Sci. USA **110**, 6736 (2013).

[15] Without a gauge field the quantum particle in 1D and 2D parabolic lattices was discussed earlier in a number of papers; see, for example, [16,17] and references therein.

[16] J. Brand and A. R. Kolovsky, Eur. Phys. J. D **7**, 331 (2007).

[17] M. Snoek and W. Hofstetter, Phys. Rev. A **76**, 051603(R) (2007).

[18] A. R. Kolovsky and G. Mantica, Phys. Rev. E **83**, 041123 (2011); A. R. Kolovsky, I. Chesnokov, and G. Mantica, *ibid.* **86**, 041146 (2012).

[19] A. R. Kolovsky and G. Mantica, Phys. Rev. B **86**, 054306 (2012).

[20] F. Gerbier and J. Dalibard, New J. Phys. **12**, 033007 (2010).

[21] C. G. Darwin, Proc. Cambridge Philos. Soc. **27**, 86 (1931).

[22] Note that, like the critical energy E_{cr} from Eq. (3) in the quantum case, the classical parameter $\tilde{\gamma}/J = \frac{J}{2E_R}(\frac{\omega_{hc}}{\omega_\alpha})^2$ is determined by the ratio between cyclotron and trap frequency.

[23] In the directions parallel to **F** the localization length of the Landau-Stark scales as $\xi_\parallel \sim J/F$, i.e., the same wave as the localization length of the Wannier-Stark states ($\alpha = 0$).

[24] R. B. Laughlin, Phys. Rev. B **23**, 5632 (1981).

[25] In the following discussion we take a convention that we ignore tiny avoided crossing. Without this convention every energy level of the system (21) is a periodic function of θ.

[26] We would like to remind the reader at this point that the high-energy region is entered through a crossover rather than a sharp transition. In the right-most panel of Fig. 11, although an energy regime below the critical energy $E_{cr} \approx 11J$ is shown, already most of the states show signatures characteristic for high energies.